AIAA JOURNAL
Vol. 40, No. 12, December 2002

Interlaminar Stress Analysis of Shell Structures with Piezoelectric Patch Including Thermal Loading

Heung Soo Kim,* Xu Zhou,* and Aditi Chattopadhyay†
Arizona State University, Tempe, Arizona 85287-6106

Interlaminar stress distribution in smart composite shells using a coupled thermal–piezoelectric–mechanical model is investigated. To maintain local accuracy of stress distributions, the trial displacement field is assumed layerwise higher order and C_0 continuous through the entire laminate thickness, accommodating zigzag in-plane warping and interlaminar shear stress continuity. The temperature and electrical fields are modeled using higher-order descriptions that can satisfy surface flux boundary conditions at structural surfaces and equipotential conditions at electrode surfaces. These assumptions ensure computational efficiency. A variational principle, addressing the interaction between thermal, piezoelectric, and mechanical fields, is used to derive the governing equations of equilibrium. The proposed theory is used to investigate the cylindrical bending problem of simply supported composite host structures with attached piezoelectric actuators, subject to a combination of mechanical, piezoelectric, and thermal loading. The interlaminar stress distributions under comprehensive loading are presented for different geometries and stacking sequences. The effects of two-way piezoelectric and thermal coupling on the stress distributions are investigated. The significance of the thermal mismatch effect on interlaminar stress distribution is also discussed. The results from present theory are validated with available exact elasticity solutions.

Nomenclature

$A_i^k(z)$, $B_i^k(z)$, $C_i^{kj}(z)$	=	layerwise coefficient functions
A_α, A_β	=	Lamè parameters
$\boldsymbol{B}_u$, $\boldsymbol{B}_\varepsilon$, $\boldsymbol{B}_\phi^j$, $\boldsymbol{B}_E^j$, $\boldsymbol{B}_\theta$, $\boldsymbol{B}_p$	=	operator matrices
$\boldsymbol{F}_u$, $\boldsymbol{F}_\phi$, $\boldsymbol{F}_\theta$	=	element force vector
$f_i(z)$, $g_i(z)$	=	through-the-thickness functions
H	=	total thickness
h_c	=	composite thickness
h_p	=	piezoelectric thickness
$\boldsymbol{K}_{uu}$, $\boldsymbol{K}_{u\phi}$, $\boldsymbol{K}_{u\theta}$, $\boldsymbol{K}_{\phi u}$, $\boldsymbol{K}_{\phi\phi}$, $\boldsymbol{K}_{\phi\theta}$, $\boldsymbol{K}_{\theta\theta}$	=	element stiffness matrix
$\boldsymbol{L}_u$, $\boldsymbol{L}_\varepsilon$, $\boldsymbol{L}_\phi^j$, $\boldsymbol{L}_E^j$, $\boldsymbol{L}_\theta$, $\boldsymbol{L}_p$	=	higher-order operator matrices
$\boldsymbol{N}_u(\alpha, \beta)$, $\boldsymbol{N}_\phi(\alpha, \beta)$, $\boldsymbol{N}_\theta(\alpha, \beta)$	=	interpolation matrices
R	=	radius of cylindrical shell
R_α, R_β	=	principal curvature radii of the α and β curves
S	=	thickness ratio (L/H for plate and R/H for shell)
$\bar{t}_i$, $\bar{q}_e$, $\bar{q}_s$	=	prescribed surface traction, charge, and heat flux
$U_i^k(\alpha, \beta, z)$, $U_z^k(\alpha, \beta, z)$	=	displacement field function
u_i, w, ϕ_i, θ_i^k, ψ_i^k, φ_i^j	=	displacement and layerwise variables
$\boldsymbol{u}_u^e$, $\boldsymbol{u}_\phi^e$, $\boldsymbol{u}_\theta^e$	=	element nodal unknowns
α, β	=	curvature coordinates along reference surface
ε, ε_{ij}	=	strain vector and tensor
$\theta(\alpha, \beta, z)$	=	higher-order temperature field
σ_{ij}	=	stresses
$\phi^j(\alpha, \beta, z)$	=	electric potential field for the jth layer

Subscripts and Superscript

i	=	α, β
i, j	=	α, β, z
$[T]$	=	transpose

Received 2 July 2001; revision received 9 July 2002; accepted for publication 24 July 2002.

*Graduate Research Associate, Department of Mechanical and Aerospace Engineering.
†Professor, Department of Mechanical and Aerospace Engineering.

I. Introduction

THE concept of smart structures, such as piezoelectric laminates, has recently received a great deal of attention as an alternative to conventional techniques. These advanced structures can be designed to react to disturbance forces actively to improve the level of performance while maintaining structural integrity. Approximations of these concepts in advanced aerospace structural applications appear to be very promising. However, the introduction of smart devices in host structures inevitably perturbs the local values of the field variables, nucleating damage such as debonding and delamination at the interface of piezoelectric devices and the host structure due to stress concentration. The layerwise characteristics of composite laminates make the determination of stress and strain distribution a challenging problem. Conventionally, classical laminate theory (CLT), which ignores transverse shear effects,[1] has been extended to smart laminated structures. Huang and Wu[2] used first-order shear deformation theory for a multilayered piezoelectric composite plate. A refined hybrid plate theory was proposed to predict the response of smart composites without shear correction factors by Mitchell and Reddy.[3] A higher-order theory was used by Chattopadhyay and Gu[4] and Chattopadhyay and Seeley[5] in the analysis of laminated structures to address transverse shear effects. The theory proved to be successful in the global analysis of moderately thick structures and smart structures. However, it fails to provide continuous distribution of transverse shear stresses. This implies that the theory is not sufficient in predicting local information regarding stress and strain distributions, which is critical in the investigation of structural integrity.

The multifield characteristics of piezoelectric structures make the analysis even more complex, particularly in the presence of thermal effects as dictated by specific missions. A typical environment is represented by a solar flux of 1350 W/m^2 as vehicles move from shadow to sunlight. Some research in the field of smart structural modeling in the presence of thermal effects has been reported.[6–10] However, one-way coupling that only considers the effect of a known

field on another field was used in Refs. 6–10. The two-way coupling between piezoelectric and mechanical fields was included in the hybrid plate theory developed by Mitchell and Reddy.[3] A coupled thermal–piezoelectric–mechanical (T–P–M) model was developed by Chattopadhyay and Gu,[11] Chattopadhyay et al.,[12] and Zhou et al.[13] to address the two-way coupling issues associated with smart composites under thermal loads. Their work indicates that the effects of two-way coupling on structural deformation increase with the thickness of the piezoelectric device. However, an equivalent single-layer approach was used, and, therefore, the localized interlaminar characteristics could not be addressed accurately by this theory.

The present paper aims at the investigation of interlaminar stress distributions in laminated shell structures using a coupled T–P–M model. The goal is to develop a theory that is capable of providing sufficient accuracy while guaranteeing computational efficiency compared to other layerwise theories. To maintain local accuracy of stress and strain distributions, the trial displacement field is assumed using zigzag functions and C_0 continuity through the entire laminate thickness, accommodating zigzag in-plane warping and interlaminar transverse shear stress continuity. The continuity conditions of in-plane displacement and transverse shear stress fields, as well as traction-free boundary conditions, are applied to reduce the number of primary structural variables. Thus, contrary to other layerwise theory, the number of independent variables in the present theory is independent of the number of layers in the laminate. The temperature and electrical fields are assumed using higher-order functions. These descriptions can satisfy surface boundary conditions of heat flux and electrical potential. The mathematical model is implemented using a finite element technique. The effectiveness and accuracy of the proposed theory are compared with exact elasticity solutions. The case of cylindrical bending and spherical composite shell structures with piezoelectric [lead zirconate titanate (PZT)] patches are investigated. The analysis of stress distributions under electrical and thermoelectrical loading is performed, and numerical results are presented.

II. Model Development

For an elastic system with piezoelectric materials, the linear constitutive relations can be expressed as follows:

$$\sigma_{ij} = c_{ijkl}\varepsilon_{kl} - e_{ijk}E_k - k_{ij}\theta, \qquad D_i = e_{ijk}\varepsilon_{jk} + b_{ij}E_j + d_i\theta \quad (1)$$

where the quantities ε_{ij} and σ_{ij} denote the components of the strain and stress tensors, respectively. The quantities E_i and D_i denote components of the electric field and electric displacement, respectively, and θ denotes the temperature rise from the initial temperature. In Eq. (1), five sets of material coefficients are used to address constitutive characteristics of mechanical, electrical, and thermal fields, as well as the coupling between these fields. The quantities c_{ijkl}, e_{ijk}, and b_{ij} represent elastic constants, piezoelectric constants, and dielectric permittivity, respectively. The quantities k_{ij} and d_i refer to thermal–mechanical and thermal–piezoelectric coupling constants, respectively.

A. Improved Shear Deformation Theory

Consider a shell element with N laminas described in orthogonal coordinates α and β along the shell midsurface, as shown in Fig. 1.

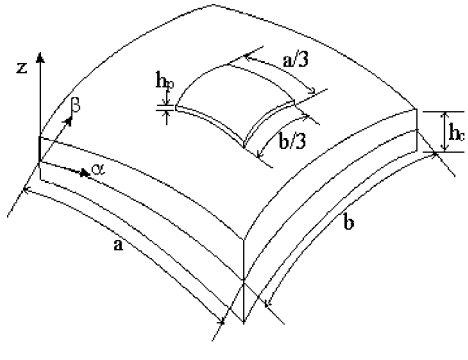

Fig. 1 Geometry of spherical shell with patched PZTs.

The thickness coordinate z is measured from the midsurface, and R_α and R_β are the radii of curvature of the α and β curves. The area of an infinitesimal rectangle $\mathrm{d}S$ and the volume of an infinitesimal parallelepiped $\mathrm{d}v$ are defined as follows:

$$\mathrm{d}S = A_\alpha(1 + z/R_\alpha)A_\beta(1 + z/R_\beta)\,\mathrm{d}\alpha\,\mathrm{d}\beta$$

$$\mathrm{d}v = A_\alpha(1 + z/R_\alpha)A_\beta(1 + z/R_\beta)\,\mathrm{d}\alpha\,\mathrm{d}\beta\,\mathrm{d}z \quad (2)$$

where A_α and A_β are the coefficients of the first fundamental form of the shell reference surface. In the present paper, the equilibrium of the shell element is described using layerwise functions as follows: For the composite layer,

$$U_\alpha^k(\alpha,\beta,z) = (1 + z/R_\alpha)u_\alpha(\alpha,\beta) + z\phi_\alpha(\alpha,\beta) + f_\alpha(z)\theta_\alpha^k(\alpha,\beta) + g_\alpha(z)\psi_\alpha^k(\alpha,\beta)$$

$$U_\beta^k(\alpha,\beta,z) = (1 + z/R_\beta)u_\beta(\alpha,\beta) + z\phi_\beta(\alpha,\beta) + f_\beta(z)\theta_\beta^k(\alpha,\beta) + g_\beta(z)\psi_\beta^k(\alpha,\beta)$$

$$U_z^k(\alpha,\beta,z) = w(\alpha,\beta) \quad (3)$$

For the PZT layer,

$$U_\alpha^k(\alpha,\beta,z) = (1 + z/R_\alpha)u_\alpha(\alpha,\beta) + z\phi_\alpha(\alpha,\beta) + f_\alpha(z)\theta_\alpha^k(\alpha,\beta) + g_\alpha(z)\psi_\alpha^k(\alpha,\beta) + z\varphi_\alpha^i(\alpha,\beta)$$

$$U_\beta^k(\alpha,\beta,z) = (1 + z/R_\beta)u_\beta(\alpha,\beta) + z\phi_\beta(\alpha,\beta) + f_\beta(z)\theta_\beta^k(\alpha,\beta) + g_\beta(z)\psi_\beta^k(\alpha,\beta) + z\varphi_\beta^i(\alpha,\beta)$$

$$U_z^k(\alpha,\beta,z) = w(\alpha,\beta) \quad (4)$$

Equations (3) and (4) describe the zigzag in-plane deformation using a combination of laminatewise first-order shear deformation theory and layerwise higher-order rotation. In these equations, a superscript k denotes the kth layer of the laminate, and superscript i denotes the ith PZT layer. Laminate unknowns (u_α, u_β, ϕ_α, and ϕ_β) and layerwise unknowns (θ_α^k, θ_β^k, ψ_α^k, and ψ_β^k) are used to address in-plane deformation. Rotational degrees of freedom (φ_α^i and φ_α^i) are introduced in the PZT layer to describe electrical actuation. The through-the-laminate thickness functions, $f_\alpha(z)$, $f_\beta(z)$, $g_\alpha(z)$, and $g_\beta(z)$ are used to address the characteristics of in-plane zigzag deformation and have the following form:

$$f_\alpha(z) = f_\beta(z) = \sinh(z), \qquad g_\alpha(z) = g_\beta(z) = \cosh(z) \quad (5)$$

where the functions $f_\alpha(z)$, $f_\beta(z)$, $g_\alpha(z)$, and $g_\beta(z)$ render higher-order odd and even distributions, respectively. Note that Eqs. (3) and (4) result in a $4N + 5 + 2N_p$ number of structural unknowns in the displacement field, where N is the total number of layers and N_p is the number of PZT layers. Thus, the assumed displacement field can allow for discontinuous transverse shear strain at the laminate interfaces; however, the total number of structural variables is dependent on the number of laminas. This implies increased computational effort if multilayered laminates are used. Thus, a procedure is developed to reduce the number of structural unknowns. This involves the imposition of conditions of free transverse shear stress on the top and the bottom surfaces and the conditions of continuous transverse shear stress and in-plane displacement at interlaminar surfaces. The details of the procedure are described in Ref. 14. A linear strain–displacement relationship[15] is used, and only cross-ply laminates are considered in the present paper. The displacement field can now be written as

$$U_\alpha^k = \left(1 + \frac{z}{R_\alpha}\right)u_\alpha + A_\alpha^k(z)\phi_\alpha + B_\alpha^k(z)w_{,\alpha} + \sum_i^{N_p} C_\alpha^{k^i}(z)\varphi_\alpha^i$$

$$U_\beta^k = \left(1 + \frac{z}{R_\beta}\right)u_\beta + A_\beta^k(z)\phi_\beta + B_\beta^k(z)w_{,\beta} + \sum_i^{N_p} C_\beta^{k^i}(z)\varphi_\beta^i$$

$$U_z^k = w \quad (6)$$

where the layerwise coefficient functions are expressed as follows: For the composite layer,

$$A_\alpha^k(z) = a_{\alpha 1}^k f_\alpha(z) + a_{\alpha 2}^k g_\alpha(z) + z$$
$$A_\beta^k(z) = a_{\beta 1}^k f_\beta(z) + a_{\beta 2}^k g_\beta(z) + z$$
$$B_\alpha^k(z) = b_{\alpha 1}^k f_\alpha(z) + b_{\alpha 2}^k g_\alpha(z), \qquad B_\beta^k(z) = b_{\beta 1}^k f_\beta(z) + b_{\beta 2}^k g_\beta(z)$$
$$C_\alpha^{k^i}(z) = c_{\alpha 1}^{k^i} f_\alpha(z) + c_{\alpha 2}^{k^i} g_\alpha(z), \qquad C_\beta^{k^i}(z) = c_{\beta 1}^{k^i} f_\beta(z) + c_{\beta 2}^{k^i} g_\beta(z) \tag{7}$$

For the PZT layer,

$$A_\alpha^k(z) = a_{\alpha 1}^k f_\alpha(z) + a_{\alpha 2}^k g_\alpha(z) + z$$
$$A_\beta^k(z) = a_{\beta 1}^k f_\beta(z) + a_{\beta 2}^k g_\beta(z) + z$$
$$B_\alpha^k(z) = b_{\alpha 1}^k f_\alpha(z) + b_{\alpha 2}^k g_\alpha(z)$$
$$B_\beta^k(z) = b_{\beta 1}^k f_\beta(z) + b_{\beta 2}^k g_\beta(z)$$
$$C_\alpha^{k^i}(z) = c_{\alpha 1}^{k^i} f_\alpha(z) + c_{\alpha 2}^{k^i} g_\alpha(z) + z\delta_i$$
$$C_\beta^{k^i}(z) = c_{\beta 1}^{k^i} f_\beta(z) + c_{\beta 2}^{k^i} g_\beta(z) + z\delta_i$$
$$\text{if} \quad z_i \le z \le z_{i+1} \qquad \delta_i = 1$$
$$\text{else} \quad \delta_i = 0 \tag{8}$$

In Eqs. (7) and (8), the layerwise coefficients ($a_{\alpha 1}^k$, $b_{\alpha 1}^k$, and so on) are obtained by enforcing a displacement and stress continuity condition at each interface and traction-free boundary conditions at free surfaces. Note that the structural unknowns describing the mechanical field, ranging from the first lamina to the Nth lamina, are reduced to a total of variables, $5 + 2N_p$, which are u_α, u_β, w, ϕ_α, ϕ_β, φ_α^i, and φ_β^i. Therefore, the developed approach renders the number of structural variables independent of the number of lamina but dependent on the number of PZT layers. All terms on the order of the thickness coordinate to radius are retained in the formulation, which makes the current approach applicable to the analysis of thick-shell structures.

B. Higher-Order Piezoelectric Field

The field of electric potential must satisfy the surface boundary condition of applied voltages. Therefore, a cubic distribution of the potential field along the thickness of piezoelectric layers is assumed. The potential field ϕ^j for the jth layer can be written as follows[16]:

$$\phi^j(\alpha, \beta, z) = \phi_0^j(\alpha, \beta) - \left(z - z_0^j\right) E_z^j(\alpha, \beta) + 4\left[\left(z - z_0^j\right)/h^j\right]^2 \times \left\{\left(z - z_0^j\right)\left[(\bar{\phi}^j/h^j) + E_z^j(\alpha, \beta)\right] - \phi_0^j(\alpha, \beta)\right\} \tag{9}$$

where ϕ_0^j is the potential of a point in the midplane of the jth piezoelectric layer. The quantity E_z^j denotes the electric field at midplane and the term $-(z - z_0^j)E_z^j$ is used to address the linear potential distribution along the thickness. The last term in Eq. (9) represents the higher-order modification, addressing the nonuniform potential variation through the thickness while satisfying the equipotential surface boundary conditions prescribed at the electrodes. The quantity $\bar{\phi}^j$ denotes the potential difference between the top and the bottom electrodes covering the jth piezoelectric transducer, and z_0^j and h^j denote the midplane position and the thickness of the jth piezoelectric layer, respectively.

C. Higher-Order Temperature Field

The temperature field must satisfy the surface boundary condition of the heat flux accurately. To address nonuniform temperature distribution through the laminate thickness, the temperature field is described using a cubic function of the thickness coordinate. By the imposition of the surface boundary conditions of the heat flux, the higher-order temperature field can be written as follows[12,13]:

$$\theta(\alpha, \beta, z) = -\left\{(z^2/2H)[(q_t - q_b)/\kappa_{33}] + (2z^3/3H^2)[(q_t + q_b)/\kappa_{33}]\right\} + \theta_0(\alpha, \beta) + [z - (4/3H^2)z^3]\theta_1(\alpha, \beta) \tag{10}$$

where the quantities q_t and q_b indicate the heat flux applied on the top and bottom surfaces, respectively. The quantity κ_{33} denotes thermal conductivity through the thickness and H represents the total thickness of the laminate. The higher-order temperature field defines a nonuniform cubic distribution through the thickness of the structure. Note that, although a linear temperature filed can address the in-plane temperature distribution, it cannot satisfy the surface thermal boundary conditions. Thus, temperature variations through the thickness, which produce the most important bending deformation, cannot be modeled accurately using a linear temperature field.

III. Finite Element Implementation

The finite element implementation of a shell element with piezoelectric layers using a T–P–M coupled model is presented in this section. The displacement and temperature unknowns of the element are denoted $\boldsymbol{u}_u^e$ and $\boldsymbol{u}_\theta^e$, respectively. The electrical unknowns of the jth piezoelectric layer are denoted $\boldsymbol{u}_\phi^{e,j}$. The displacement field in the midplane of the host structures and the ith piezoelectric layer $[\boldsymbol{u}_{u0}(\alpha, \beta)]$, the electrical field in the midplane of the jth piezoelectric layer $[\boldsymbol{u}_{\phi 0}^j(\alpha, \beta)]$, and the temperature field in the midplane of the element $[\boldsymbol{u}_{\theta 0}(\alpha, \beta)]$ can be expressed using appropriate interpolation functions, as follows:

$$\boldsymbol{u}_{u0}(\alpha, \beta) = \left[u_\alpha, u_\beta, \phi_\alpha, \phi_\beta, w, \varphi_\alpha^i, \varphi_\beta^i\right]^T = \boldsymbol{N}_u(\alpha, \beta)\boldsymbol{u}_u^e$$
$$\boldsymbol{u}_{\phi 0}^j(\alpha, \beta) = \left[\phi_0^j, E_z^j\right]^T = \boldsymbol{N}_\phi(\alpha, \beta)\boldsymbol{u}_\phi^{e,j}$$
$$\boldsymbol{u}_{\theta 0}(\alpha, \beta) = [\theta_0, \theta_1]^T = \boldsymbol{N}_\theta(\alpha, \beta)\boldsymbol{u}_\theta^e \tag{11}$$

where $\boldsymbol{N}_u(\alpha, \beta)$, $\boldsymbol{N}_\phi(\alpha, \beta)$, and $\boldsymbol{N}_\theta(\alpha, \beta)$ are the interpolation functions describing displacement, potential, and temperature field, respectively. The element displacement field $\boldsymbol{u}(\alpha, \beta, z)$, the strain $\varepsilon(\alpha, \beta, z)$, the potential field $\phi^j(\alpha, \beta, z)$, the electric field $\boldsymbol{E}^j(\alpha, \beta, z)$, the temperature field $\theta(\alpha, \beta, z)$, and the gradient of the temperature field $\theta_{,i}(\alpha, \beta, z)$ are defined in Appendix A.

The linear thermoelectromechanical multiple field problem for a domain V without free body charge, based on displacement, electric potential, and temperature as independent state variables, can be described using variational principle along with several constraints, as follows:

$$\delta\pi(u_i, \phi, \theta) = \int_V (\sigma_{ij}\delta\varepsilon_{ij} - D_i\delta\phi_{,i} + \kappa_{ij}\theta_{,i}\,\delta\theta_{,j})\,\mathrm{d}V - \int_{\Gamma_\sigma} \bar{t}_i\delta u_i\,\mathrm{d}\Gamma + \int_{\Gamma_D} \bar{q}_e\delta\phi\,\mathrm{d}\Gamma + \int_{\Gamma_q} \bar{q}_s\delta\theta\,\mathrm{d}\Gamma = 0 \tag{12}$$

Equation (12) addresses temperature and piezoelectric and mechanical fields simultaneously and represents the governing equations of the coupled T–P–M theory. The quantities $\bar{t}_i$, $\bar{q}_e$, and $\bar{q}_s$ denote the prescribed traction on the stress boundary Γ_σ, surface charge on the charge boundary Γ_D, and surface heat flux on the flux boundary Γ_q, respectively.

When Eq. (A1) is substituted into Eq. (12), the following finite element governing equations of the T–P–M coupled theory are obtained:

$$\begin{bmatrix} \boldsymbol{K}_{uu} & \boldsymbol{K}_{u\phi} & \boldsymbol{K}_{u\theta} \\ \boldsymbol{K}_{\phi u} & \boldsymbol{K}_{\phi\phi} & \boldsymbol{K}_{\phi\theta} \\ 0 & 0 & \boldsymbol{K}_{\theta\theta} \end{bmatrix} \begin{Bmatrix} \boldsymbol{u}_u^e \\ \boldsymbol{u}_\phi^e \\ \boldsymbol{u}_\theta^e \end{Bmatrix} = \begin{Bmatrix} \boldsymbol{F}_u \\ \boldsymbol{F}_\phi \\ \boldsymbol{F}_\theta \end{Bmatrix} \tag{13}$$

where the matrices $\boldsymbol{K}_{u\phi}$ and $\boldsymbol{K}_{\phi u}$ are stiffness matrices due to piezoelectric–mechanical coupling, and $\boldsymbol{K}_{u\theta}$ and $\boldsymbol{K}_{\phi\theta}$ are stiffness matrices due to thermal–mechanical and thermal–electrical coupling, respectively. The matrices $\boldsymbol{K}_{uu}$, $\boldsymbol{K}_{\phi\phi}$, and $\boldsymbol{K}_{\theta\theta}$ are stiffness matrices due to mechanical, electrical, and thermal fields, respectively. The vectors $\boldsymbol{F}_u$, $\boldsymbol{F}_\phi$, and $\boldsymbol{F}_\theta$ are force vectors due to mechanical, electrical, and thermal fields, respectively. The stiffness matrices and force vectors are defined in Appendix B.

IV. Results and Discussion

The effectiveness and accuracy of the proposed displacement field theory is evaluated by comparison with other theories. First, the bending of a composite plate with top and bottom actuators, as

Table 1 Material properties of PZT and graphite/epoxy composite

Parameter	PZT	Graphite/epoxy
	Elastic moduli, GPa	
E_{11}	2.0	172.5
E_{22}	2.0	6.9
E_{33}	2.0	6.9
	Shear moduli, GPa	
G_{23}	1.41	3.45
G_{13}	1.41	1.38
G_{12}	1.41	1.38
	Poisson's ratio	
ν	0.29	0.25
	Coefficients of thermal expansion, $\mu m/m \cdot {}^\circ C$	
α_{11}	0.9	1.1
α_{33}	0.9	25.2
	Piezoelectric charge constant c/m^2	
$e_{31} = e_{32}$	0.046	——
	Electric permittivity, nf/m	
b_{11}	15.0	——
b_{33}	15.0	——
	Pyroelectric constant, $\mu C/m^2 \cdot {}^\circ C$	
d_3	20	——
	Thermal conductivity, $W/m \cdot {}^\circ C$	
κ_{11}	2.1	4.48
κ_{33}	2.1	3.21

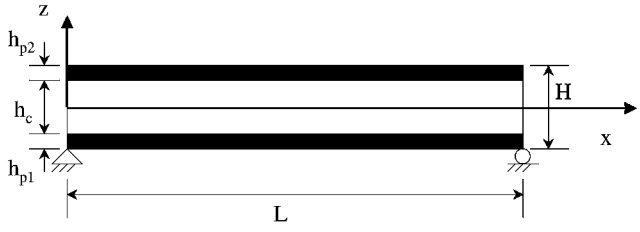

Fig. 2 Infinite plate with PZT actuators.

shown in Fig. 2, is investigated. The top and bottom layers serve as the distributed actuators. The plate is simply supported and is infinite in one direction (that is, plane strain state). The radii of curvature R_α and R_β are infinite, and the midsurface metrics A_α and A_β are 1 in the present model. The material properties of the graphite/epoxy and PZTs are adopted from Ray et al.[17] and are presented in Table 1. The results are nondimensionalized as follows:

$$\bar{\sigma}_x = \sigma_x \big/ q_0 S^2, \qquad \bar{\sigma}_{xz} = \sigma_{xz}/q_0, \qquad S = L/H \tag{14}$$

A transverse normal loading, $q_0 \sin(\pi x/L)$, is applied on the top surface. The results from the present theory are compared with the exact solution by Ray et al.[17] Figures 3a and 3b show in-plane normal stress distributions at the center of the plate in a thick and a moderately thick case. At the top surface for $S = 4$ and 10, the present results deviate by 7 and 6%, respectively, from the exact solution. Transverse shear stress distributions are presented in Fig. 3c. The maximum stress occurs at the midsurface, and the differences in maximum stress between the present model and the exact solution are less than 1%. Thus, the stress solutions from the present theory correlate very well with exact solutions.

Piezoelectric actuation is modeled by applying sinusoidal electric potential $[\phi_0^{\text{top}} = V \sin(\pi x/L)]$ at the top PZT. The magnitude of the electric voltage V is assumed to be 100 V. Electrically induced in-plane normal stress distributions at the center of the plate are shown in Figs. 4a and 4b for $S = 4$ and 10, respectively. As seen from Figs. 4a and 4b, compressive stresses occur at the interface of the composite and top piezoactuator due to contraction of the PZT. The deviation of stresses between the present model and the exact solution at the interface of the composite and top actuator are 3.7 and 1.6%, respectively. Figure 4c shows electrically induced transverse shear stress distributions at the edge of the plate. Transverse shear stress concentration is observed at the interface of the actuator and host structure due to piezoelectric actuation. In the case of a thick

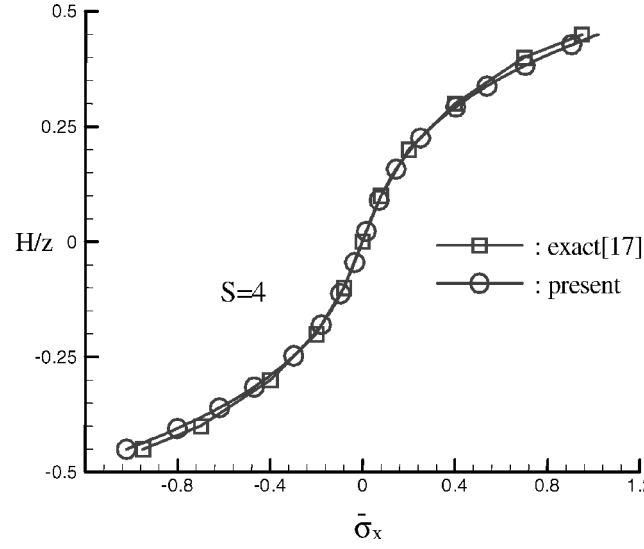

a) In-plane normal stress distribution at the center of plate, $S = 4$

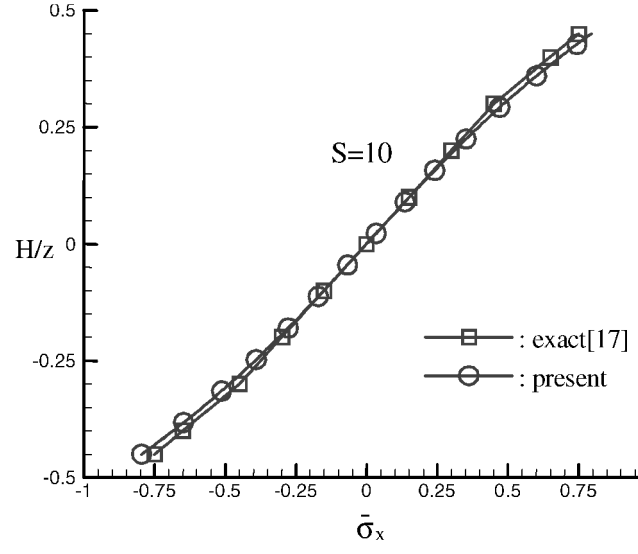

b) In-plane normal stress distribution at the center of plate, $S = 10$

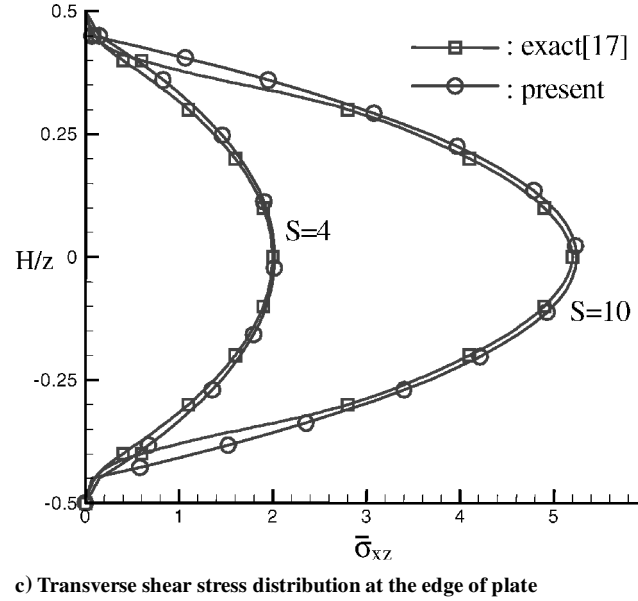

c) Transverse shear stress distribution at the edge of plate

Fig. 3 Stress distribution through the thickness direction of plate under mechanical loading.

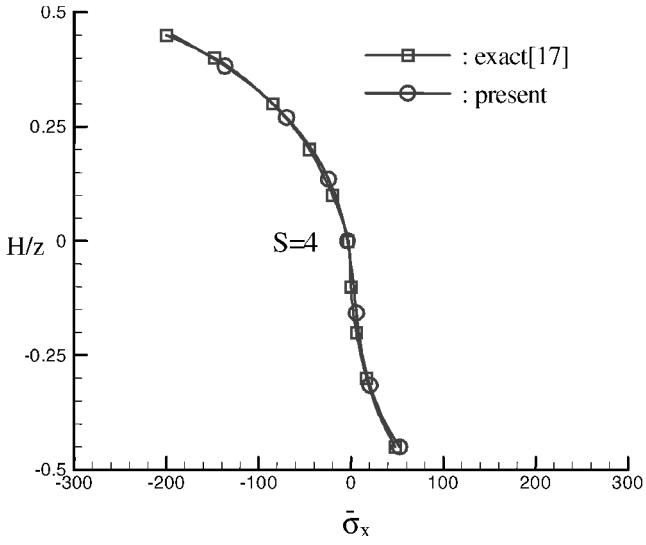

a) In-plane normal stress distribution at the center of plate, $S = 4$

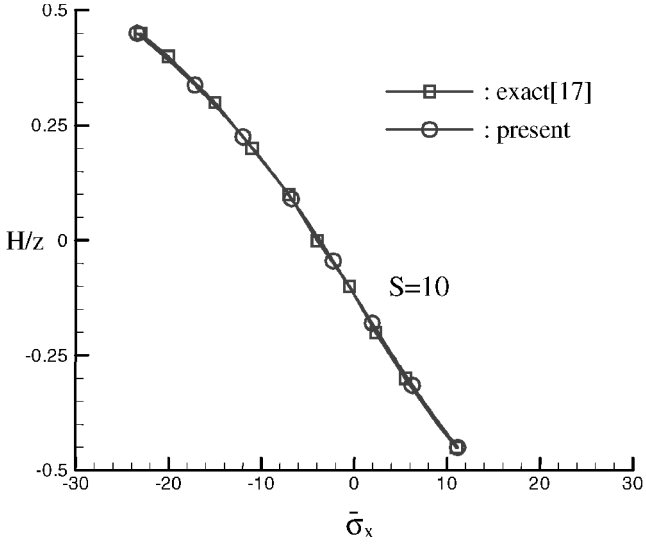

b) In-plane normal stress distribution at the center of plate, $S = 10$

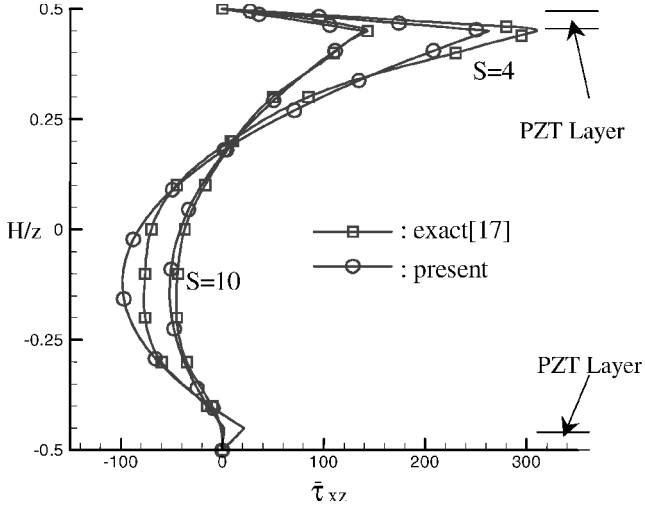

c) Transverse shear stress distribution at the edge of plate

Fig. 4 Electrically induced stress distribution through the thickness direction of plate.

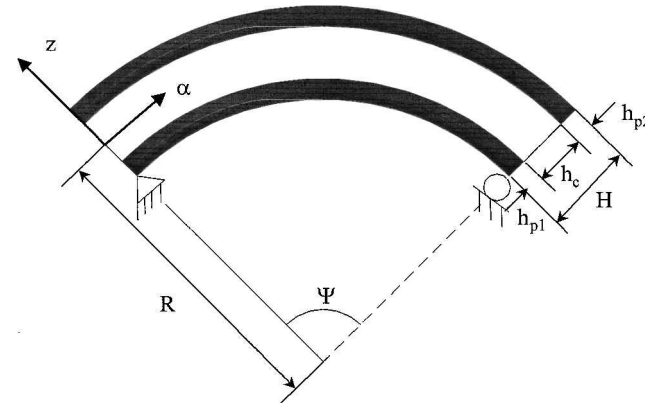

Fig. 5 Infinite cylinder with PZT actuators.

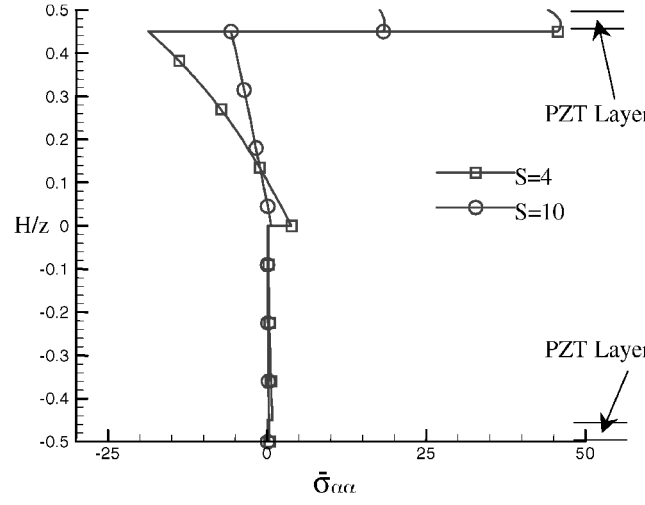

a) In-plane normal stress distribution at the center of shell

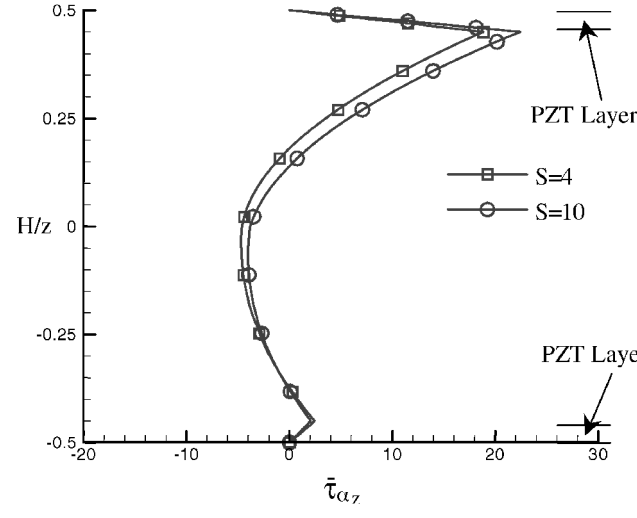

b) Transverse shear stress distribution at the edge of shell

Fig. 6 Electrically induced stress distributions through the direction of shell ([90/0]).

composite, $S = 4$, the difference in maximum shear stress is more than 10%. However, this difference is reduced to 2.5% when the thickness is reduced to $S = 10$.

Next, an infinite cylindrical shell with distributed piezoelectric actuators, as shown in Fig. 5, is considered. The radius of curvature R_α and the span angle ψ are fixed as 0.5 and $\pi/3$, respectively. The thickness of the piezoactuator is assumed to be $H/20$. The thickness ratio S is defined as R/H for the shell and the results are presented based on the same nondimensionalization as in the preceding example. The same electric potential is applied on the top actuator only. Figure 6 shows stress distributions of antisymmetric

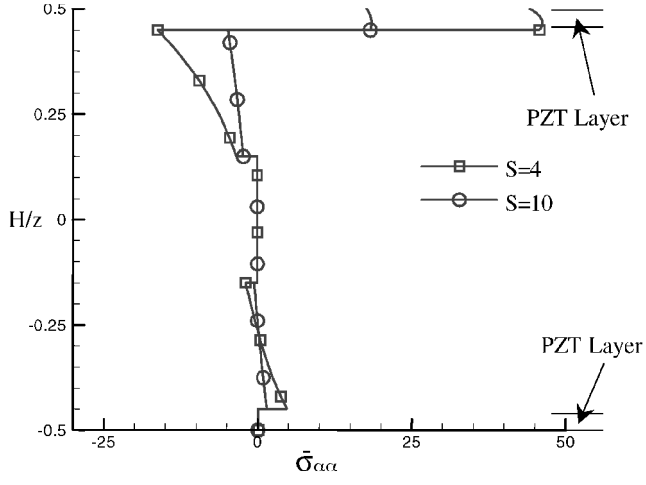

a) In-plane normal stress distribution at the center of shell

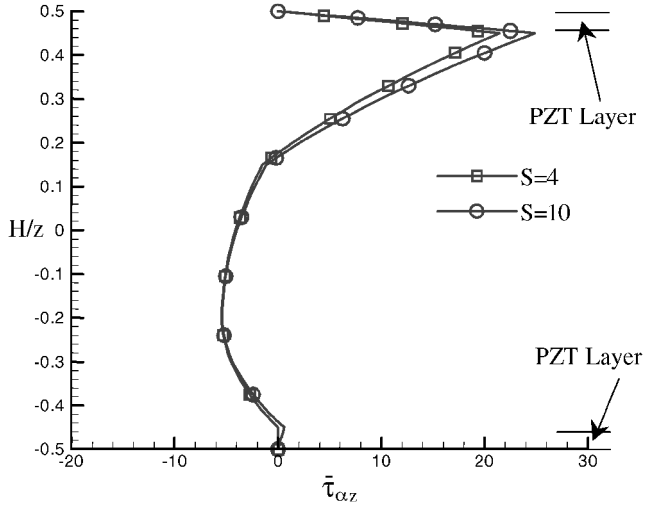

b) Transverse shear stress distribution at the edge of shell

Fig. 7 Electrically induced stress distributions through the direction of shell ([0/90/0]).

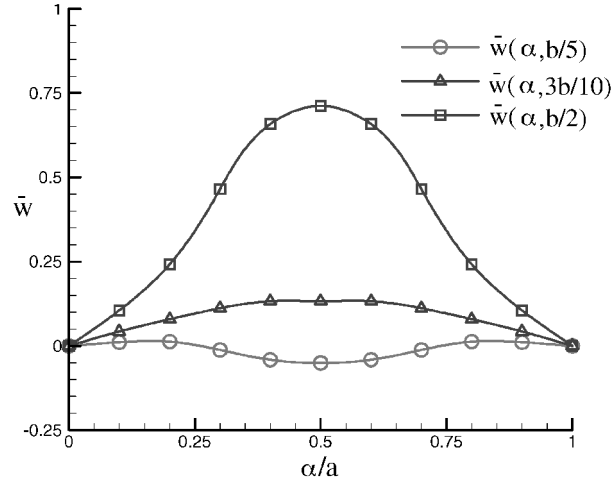

a) Deflection along α direction

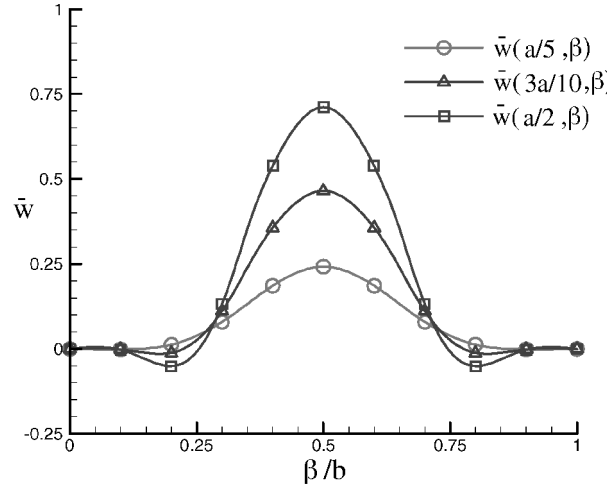

b) Deflection along β direction

Fig. 8 Electrically induced deflection at the midsurface of laminated spherical shell.

laminates [90/0]. Electrically induced in-plane normal stress distributions, for different S values, are presented in Fig. 6a. Because of the contraction of the top actuator, compressive stresses are induced at the interface between the top actuator and the host structure. The variation in induced axial compressive stress, in the upper half of the host structure, becomes nonlinear as the shell becomes thicker. The distribution of transverse shear stresses is shown in Fig. 6b. The maximum stress occurs at the interface of the actuator and the composite. The induced transverse shear changes from positive to negative through the thickness. Stress distributions in a symmetric [0/90/0] laminate are presented in Fig. 7. The trends in induced in-plane normal and transverse shear stresses are similar to those of the antisymmetric laminates.

Next, numerical analysis of a spherical fiber-reinforced laminated composite shell with patched piezoelectric actuators, under various loading conditions, is considered. Two PZT patches on the top and bottom surfaces are used to produce the desired actuation capability for shape control, as shown in Fig. 1. The actuators are located at the center of the shell. The shell structure is fixed on all four sides. The dimensions of the shell are such that the radius of curvature $R = 0.5$ m, the span angle for each direction $\psi = \pi/4$, the thickness ratio $S = 10$, and the thickness of the piezo patch $h_p = H/20$. The length of each PZT patch is assumed to be one-third of the host shell.

A three-layer symmetric laminate with a stacking sequence of [0/90/0] and an equal lamina thickness is used to investigate the effects of T–P–M coupling. Only piezoelectric actuation is considered. Both the top and bottom actuators are subjected to a voltage load of the same magnitude, but opposite direction, making out-of-direction deformation dominant. A constant electric potential ($V = 100$ V) is applied. Note that in this case, the T–P–M model for actuators represents two-way mechanical–piezoelectric coupling (piezoelectric and converse piezoelectric effects), whereas a conventional induced strain model represents only one-way mechanical–piezoelectric coupling (converse piezoelectric effect). The results are normalized as follows:

$$(\bar{\sigma}_{\alpha\alpha}, \bar{\sigma}_{\beta\beta}) = (1/VS^2)(\sigma_{\alpha\alpha}, \sigma_{\beta\beta})$$
$$(\bar{\sigma}_{\alpha z}, \bar{\sigma}_{\beta z}) = (1/VS)(\sigma_{\alpha z}, \sigma_{\beta z})$$
$$\bar{w} = 1000E_{11}w/VS^4 \tag{15}$$

Electrically induced deflections are presented in Fig. 8. Note that the deflections along the α and β directions are not symmetric due to the difference in the elastic modulus. Figure 9a shows electrically induced in-plane normal stress. To make bending deformation dominant, the top actuator is extended and the bottom actuator is contracted. As a result, tensile stress is induced on the upper half and compressive stress is induced on the lower half of the host structure. It can be observed that the distributions of in-plane normal stresses are discontinuous at the layer interfaces due to material dissimilarity. For both $\sigma_{\alpha\alpha}$ and $\sigma_{\beta\beta}$, the maximum stress occurs at the interfaces of the PZT actuators and the primary structure, which makes structural integrity a critical issue in these regions. Figure 9b presents the distributions of transverse shear stress through the laminate thickness under the same electrical loading. It can be seen that the transverse shear stresses vanish at the top and the bottom surfaces and are continuous at each interlaminar surface. The distributions show a significant gradient in actuator layers.

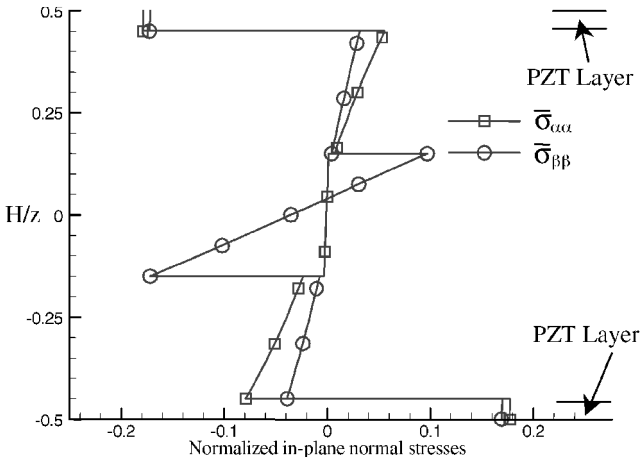

a) In-plane normal stresses

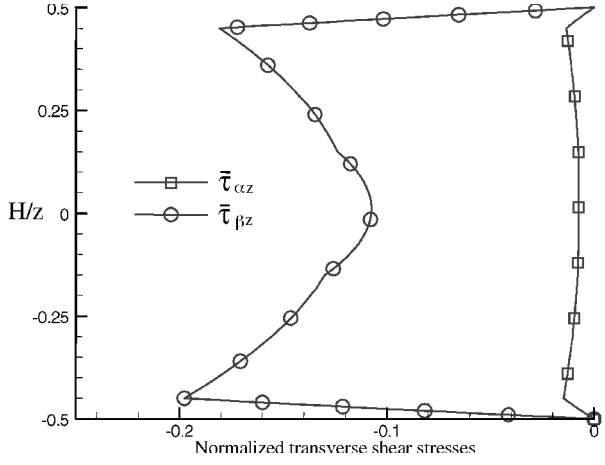

b) Transverse shear stresses

Fig. 9 Electrically induced stress distributions at the edge of PZT ($\alpha = a/3$ and $\beta = b/3$).

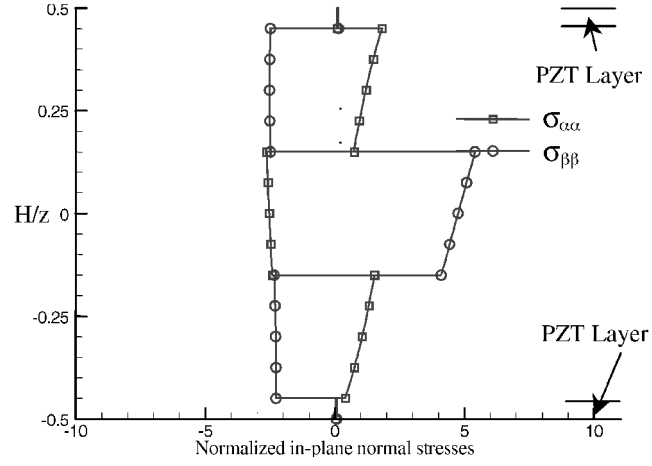

a) In-plane normal stresses

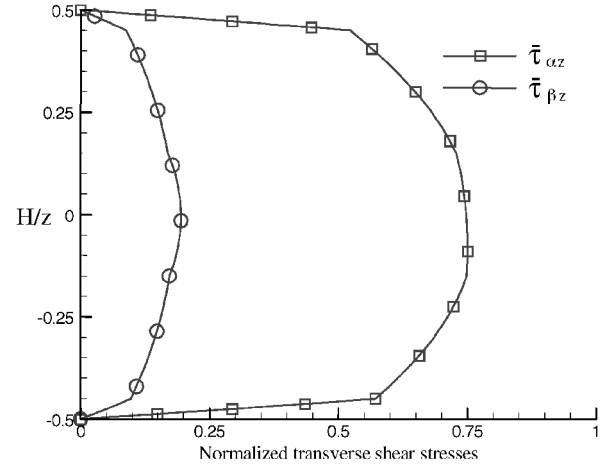

b) Transverse shear stresses

Fig. 11 Thermally induced stress distributions at the edge of PZT ($\alpha = a/3$, $\beta = b/3$).

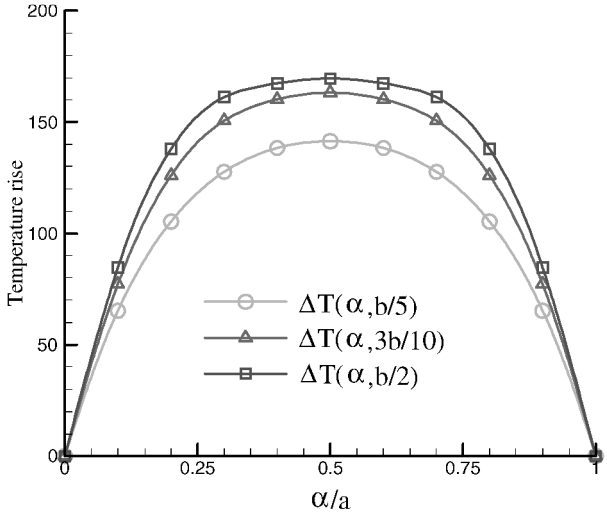

Fig. 10 Temperature rise along α direction at the midsurface.

The maximum shear stress occurs at the interfaces of the actuators and the primary structure, which makes mode 2 and mode 3 failure (both laminate delamination and actuator debonding) critical.

Next, numerical analysis with only thermal excitations is performed to investigate thermal coupling effects. The same structural configuration is used. A uniform heat flux is applied on the top surface of the structure, and it is insulated at the bottom. All four sides are maintained at room temperature (20°C). Thermal steady state is achieved when there is an equilibrium between the inflow of surface heat flux and heat outflow through the four sides of the structure. Note that although there is no external voltage, all coupling effects between thermal, piezoelectric, and mechanical fields are still present in the T–P–M model. Numerical results under a heat flux $q_t = 1000$ W/m^2 are presented in Figs. 10 and 11. Results for thermal loading are normalized as follows:

$$(\bar{\sigma}_{\alpha\alpha}, \bar{\sigma}_{\beta\beta}) = \left(1/q_t S^4\right)(\sigma_{\alpha\alpha}, \sigma_{\beta\beta})$$

$$(\bar{\sigma}_{\alpha z}, \bar{\sigma}_{\beta z}) = \left(1/q_t S^3\right)(\sigma_{\alpha z}, \sigma_{\beta z})$$

$$\bar{w} = E_{22} w / q_t S^4 \tag{16}$$

Figure 10 shows the temperature rise of the midsurface of the structure. The temperature rise in the structure is a result of the heat flow from the top surface to the side boundaries, where heat finally dissipates. The temperature rise is at a maximum at the center of the structure and has the smallest values near the structural side boundaries. The temperature distribution is also symmetric because the geometry of the shell, the thermal boundary conditions, and the external loading are all symmetric. Figures 11a and 11b present the distribution of in-plane normal stresses and transverse shear stresses, respectively. For normal stresses, the stress distribution shows discontinuity due to the mismatch of thermal material properties. For transverse shear, although the maximum stress occurs around the midsurface, the stresses at the interlaminar surfaces between the actuators and the primary structure are close to the maximum value.

V. Conclusions

An improved coupled theory is developed to address the effects of piezoelectric actuation under various kinds of loading conditions.

A new layerwise shear deformation theory, developed to accommodate the complexity of in-plane zigzag warping and continuity of transverse shear stress distribution, is used in conjunction with the completely coupled T–P–M theory. The developed theory provides a framework for accurate and efficient analysis of stress distribution in composite shell structures integrated with piezoelectric materials. Numerical analysis is performed to investigate laminated composite shells with multiple surface-bonded actuators. Piezoelectric loading and thermal loading are considered. The induced deflections and stress distributions are presented. The following important observations are made from this study:

1) The improved shear deformation theory correlates well with exact solutions. The use of the higher-order electric and temperature fields in the T–P–M model make the developed approach applicable to a large class of smart structures.

2) In the analysis of structural bending due to piezoelectric actuation, for both symmetric and antisymmetric laminations, the maximum in-plane normal and transverse shear stresses occur at the interface of the actuators and the primary structure. Thus, structural integrity becomes a critical issue in these regions.

3) In the analysis of structural bending due to thermal actuation, the results of stress analysis show that a significant thermal mismatch occurs at the interface between the actuator and the primary structure. This results in stress concentrations at these interfaces.

Appendix A: Element Field and Higher-Order Operators

Based on the described field assumptions, the element displacement field $\boldsymbol{u}(\alpha, \beta, z)$, the strain $\varepsilon(\alpha, \beta, z)$, the potential field $\phi^j(\alpha, \beta, z)$, the electric field $\boldsymbol{E}^j(\alpha, \beta, z)$, the temperature field $\theta(\alpha, \beta, z)$, and the gradient of temperature field $\theta_{,i}(\alpha, \beta, z)$ can be written as follows:

$$\begin{gathered}
\boldsymbol{u}(\alpha, \beta, z) = \boldsymbol{L}_u \boldsymbol{u}_{u0}(\alpha, \beta), \qquad \varepsilon(\alpha, \beta, z) = \boldsymbol{L}_\varepsilon \boldsymbol{u}_{u0}(\alpha, \beta) \\
\phi^j(\alpha, \beta, z) = F_\phi\left(z - z_0^j\right) + \boldsymbol{L}_\phi^j \boldsymbol{u}_{\phi 0}^j(\alpha, \beta) \\
\boldsymbol{E}^j(\alpha, \beta, z) = -\boldsymbol{F}_E\left(z - z_0^j\right) - \boldsymbol{L}_E^j \boldsymbol{u}_{\phi 0}^j(\alpha, \beta) \\
\theta(\alpha, \beta, z) = F_\theta(z) + \boldsymbol{L}_\theta \boldsymbol{u}_{\theta 0}(\alpha, \beta) \\
\theta_{,i}(\alpha, \beta, z) = \boldsymbol{F}_p(z) + \boldsymbol{L}_p \boldsymbol{u}_{\theta 0}(\alpha, \beta)
\end{gathered} \tag{A1}$$

where the higher-order operators, $\boldsymbol{L}_u$ and $\boldsymbol{L}_\varepsilon$, are defined as follows:

$$\boldsymbol{L}_u = \begin{bmatrix}
1 + \dfrac{z}{R_\alpha} & 0 & A_\alpha^k(z) & 0 & B_\alpha^k(z)\dfrac{\partial}{\partial \alpha} & C_\alpha^{k^i}(z) & 0 \\
0 & 1 + \dfrac{z}{R_\beta} & 0 & A_\beta^k(z) & B_\beta^k(z)\dfrac{\partial}{\partial \beta} & 0 & C_\beta^{k^i}(z) \\
0 & 0 & 0 & 0 & 1 & 0 & 0
\end{bmatrix} \tag{A2}$$

$$\boldsymbol{L}_\varepsilon = \begin{bmatrix}
l_{11}\dfrac{\partial}{\partial \alpha} & 0 & l_{12}\dfrac{\partial}{\partial \alpha} & 0 & l_{13} + l'_{13}\dfrac{\partial^2}{\partial \alpha^2} & l_{14}\dfrac{\partial}{\partial \alpha} & 0 \\
0 & l_{21}\dfrac{\partial}{\partial \beta} & 0 & l_{22}\dfrac{\partial}{\partial \beta} & l_{23} + l'_{23}\dfrac{\partial^2}{\partial \beta^2} & 0 & l_{24}\dfrac{\partial}{\partial \beta} \\
0 & 0 & 0 & l_{31} & l_{32}\dfrac{\partial}{\partial \beta} & 0 & l_{33} \\
0 & 0 & l_{41} & 0 & l_{42}\dfrac{\partial}{\partial \alpha} & l_{43} & 0 \\
l_{51}\dfrac{\partial}{\partial \beta} & l_{52}\dfrac{\partial}{\partial \alpha} & l_{53}\dfrac{\partial}{\partial \beta} & l_{54}\dfrac{\partial}{\partial \alpha} & l_{55}\dfrac{\partial^2}{\partial \alpha \partial \beta} & l_{56}\dfrac{\partial}{\partial \beta} & l_{57}\dfrac{\partial}{\partial \alpha}
\end{bmatrix} \tag{A3}$$

with

$$\begin{gathered}
l_{11} = 1/A_\alpha/(1 + z/R_\alpha), \qquad l_{21} = 1/A_\beta/(1 + z/R_\beta) \\
l_{12} = A_\alpha^k(z)\big/A_\alpha\big/(1 + z/R_\alpha), \qquad l_{22} = A_\beta^k(z)\big/A_\beta\big/(1 + z/R_\beta) \\
l_{13} = 1/R_\alpha/(1 + z/R_\alpha), \qquad l_{23} = 1/R_\beta/(1 + z/R_\beta) \\
l'_{13} = B_\alpha^k(z)\big/A_\alpha\big/(1 + z/R_\alpha), \qquad l'_{23} = B_\beta^k(z)\big/A_\beta\big/(1 + z/R_\beta) \\
l_{14} = C_\alpha^{k^i}(z)\big/A_\alpha\big/(1 + z/R_\alpha), \qquad l_{24} = C_\beta^{k^i}(z)\big/A_\beta\big/(1 + z/R_\beta) \\
l_{31} = A_{\beta,z}^k(z) - A_\beta^k(z)\big/R_\beta\big/(1 + z/R_\beta) \\
l_{32} = B_{\beta,z}^k(z) - B_\beta^k(z)\big/R_\beta\big/(1 + z/R_\beta) \\
l_{33} = C_{\beta,z}^{k^i}(z) - C_\beta^{k^i}(z)\big/R_\beta\big/(1 + z/R_\beta) \\
l_{41} = A_{\alpha,z}^k(z) - A_\alpha^k(z)\big/R_\alpha\big/(1 + z/R_\alpha) \\
l_{42} = B_{\alpha,z}^k(z) - B_\alpha^k(z)\big/R_\alpha\big/(1 + z/R_\alpha) \\
l_{43} = C_{\alpha,z}^{k^i}(z) - C_\alpha^{k^i}(z)\big/R_\alpha\big/(1 + z/R_\alpha) \\
l_{51} = A_\alpha(1 + z/R_\alpha)/A_\beta/(1 + z/R_\beta) \\
l_{52} = A_\beta(1 + z/R_\beta)/A_\alpha/(1 + z/R_\alpha) \\
l_{53} = A_\alpha^k(z)\big/A_\beta\big/(1 + z/R_\beta), \qquad l_{54} = A_\beta^k(z)\big/A_\alpha\big/(1 + z/R_\alpha) \\
l_{55} = B_\alpha^k(z)\big/A_\beta\big/(1 + z/R_\beta) + B_\beta^k(z)\big/A_\alpha\big/(1 + z/R_\alpha) \\
l_{56} = C_\alpha^{k^i}(z)\big/A_\beta\big/(1 + z/R_\beta), \qquad l_{57} = C_\beta^{k^i}(z)\big/A_\alpha\big/(1 + z/R_\alpha)
\end{gathered} \tag{A4}$$

The higher-order operators and functions associated with the electrical field, $\boldsymbol{L}_\phi^j$, $\boldsymbol{L}_E^j$, F_ϕ and $\boldsymbol{F}_E$, are defined as follows:

$$\boldsymbol{L}_\phi^j = \left[\frac{1 - 4\left(z - z_0^j\right)^2}{(h^j)^2}, -\left(z - z_0^j\right) + \frac{4\left(z - z_0^j\right)^3}{(h^j)^2}\right]$$

$$\boldsymbol{L}_E^j = \begin{bmatrix}
\left\{\dfrac{1 - 4\left(z - z_0^j\right)^2}{(h^j)^2}\right\}\dfrac{\partial}{\partial \alpha} & \left\{\dfrac{4\left(z - z_0^j\right)^3}{(h^j)^2} - \left(z - z_0^j\right)\right\}\dfrac{\partial}{\partial \alpha} \\
\left\{\dfrac{1 - 4\left(z - z_0^j\right)^2}{(h^j)^2}\right\}\dfrac{\partial}{\partial \beta} & \left\{\dfrac{4\left(z - z_0^j\right)^3}{(h^j)^2} - \left(z - z_0^j\right)\right\}\dfrac{\partial}{\partial \beta} \\
\dfrac{-8\left(z - z_0^j\right)}{(h^j)^2} & \dfrac{12\left(z - z_0^j\right)^2}{(h^j)^2} - 1
\end{bmatrix}$$

$$F_\phi\left(z - z_0^j\right) = \frac{4\bar{\phi}^j\left(z - z_0^j\right)^3}{(h^j)^3}$$

$$\boldsymbol{F}_E\left(z - z_0^j\right) = \left[0 \quad 0 \quad \frac{12\bar{\phi}^j\left(z - z_0^j\right)^2}{(h^j)^3}\right] \tag{A5}$$

The higher-order operators and functions associated with the thermal field, $\boldsymbol{L}_\theta$, $\boldsymbol{L}_p$, F_θ, and $\boldsymbol{F}_p$, are defined as follows:

$$\boldsymbol{L}_\theta = \lfloor 1 \quad z - 4z^3/3H^2 \rfloor$$

$$\boldsymbol{L}_p = \begin{bmatrix}
\dfrac{\partial}{\partial \alpha} & \left(\dfrac{z - 4z^3}{3H^2}\right)\dfrac{\partial}{\partial \alpha} \\
\dfrac{\partial}{\partial \beta} & \left(\dfrac{z - 4z^3}{3H^2}\right)\dfrac{\partial}{\partial \beta} \\
0 & \left(\dfrac{1 - 4z^2}{H^2}\right)
\end{bmatrix}$$

$$F_\theta(z) = -\left(\frac{z^2}{2H}\frac{q_t - q_b}{\kappa_{33}} + \frac{2z^3}{3H^2}\frac{q_t + q_b}{\kappa_{33}}\right)$$

$$\boldsymbol{F}_p(z) = \left[0 \quad 0 \quad \frac{\mathrm{d}F_\theta(z)}{\mathrm{d}z}\right] \tag{A6}$$

Appendix B: Stiffness Matrices, Force Vectors, and Operators

The stiffness matrices and force vectors are defined as follows:

$$\boldsymbol{K}_{uu} = \int_V \boldsymbol{B}_\varepsilon^T \boldsymbol{Q} \boldsymbol{B}_\varepsilon \, \mathrm{d}V, \qquad \boldsymbol{K}_{u\phi} = \int_V \boldsymbol{B}_\varepsilon^T \boldsymbol{P} \boldsymbol{B}_E \, \mathrm{d}V$$

$$\boldsymbol{K}_{u\theta} = -\int_V \boldsymbol{B}_\varepsilon^T \boldsymbol{k} \boldsymbol{B}_\theta \, \mathrm{d}V, \qquad \boldsymbol{K}_{\phi u} = -\boldsymbol{K}_{u\phi}^T$$

$$\boldsymbol{K}_{\phi\phi} = \int_V \boldsymbol{B}_E^T \boldsymbol{B} \boldsymbol{B}_E \, \mathrm{d}V, \qquad \boldsymbol{K}_{\phi\theta} = -\int_V \boldsymbol{B}_E^T \boldsymbol{d} \boldsymbol{B}_\theta \, \mathrm{d}V$$

$$\boldsymbol{K}_{\theta\theta} = \int_V \boldsymbol{B}_p^T \kappa \boldsymbol{B}_p \, \mathrm{d}V$$

$$\boldsymbol{F}_u = \int_S \boldsymbol{B}_u^T \boldsymbol{t} \, \mathrm{d}S - \int_V \boldsymbol{B}_\varepsilon^T \boldsymbol{k} \left(\frac{z^2}{2H} \frac{q_t - q_b}{\kappa_{33}} + \frac{2z^3}{3H^2} \frac{q_t + q_b}{\kappa_{33}} \right) \mathrm{d}V - \int_V \boldsymbol{B}_\varepsilon^T \boldsymbol{P} \boldsymbol{F}_b \left(z - z_0^j \right) \mathrm{d}V$$

$$\boldsymbol{F}_\phi = -\int_S \boldsymbol{B}_\phi^T q_e \, \mathrm{d}S - \int_V \boldsymbol{B}_E^T \boldsymbol{B} \boldsymbol{F}_b \left(z - z_0^j \right) \mathrm{d}V - \int_V \boldsymbol{B}_\phi^T \boldsymbol{d} \left(\frac{z^2}{2H} \frac{q_t - q_b}{\kappa_{33}} \frac{2z^3}{3H^2} \frac{q_t + q_b}{\kappa_{33}} \right) \mathrm{d}V$$

$$\boldsymbol{F}_\theta = -\int_S \boldsymbol{B}_\theta^T q_t \, \mathrm{d}S - \int_V \boldsymbol{B}_p^T \kappa \boldsymbol{F}_p(z) \, \mathrm{d}V \tag{B1}$$

with the definition of the operators as follows:

$$\boldsymbol{B}_u = \boldsymbol{L}_u \boldsymbol{N}_u(\alpha, \beta), \qquad \boldsymbol{B}_\varepsilon = \boldsymbol{L}_\varepsilon \boldsymbol{N}_u(\alpha, \beta), \qquad \boldsymbol{B}_\phi^j = \boldsymbol{L}_\phi^j \boldsymbol{N}_\phi(\alpha, \beta)$$

$$\boldsymbol{B}_E^j = \boldsymbol{L}_E^j \boldsymbol{N}_\phi(\alpha, \beta), \qquad \boldsymbol{B}_\theta = \boldsymbol{L}_\theta \boldsymbol{N}_\theta(\alpha, \beta), \qquad \boldsymbol{B}_p = \boldsymbol{L}_p \boldsymbol{N}_\theta(\alpha, \beta) \tag{B2}$$

Acknowledgments

The research is supported by NASA Langley Research Center Grant NAG-1-2283, Technical Monitor D. Ambur.

References

[1]Crawley, E. F., and de Luis, J., "Use of Piezoelectric Actuators as Elements of Intelligent Structures," *AIAA Journal*, Vol. 25, No. 10, 1987, pp. 1373–1385.

[2]Huang, J. H., and Wu, T., "Analysis of Hybrid Multilayered Piezoelectric Plates," *International Journal of Engineering Science*, Vol. 34, No. 2, 1996, pp. 171–181.

[3]Mitchell, J. A., and Reddy, J. N., "A Refined Hybrid Plate Theory for Composite Laminates with Piezoelectric Laminae," *International Journal of Solids Structure*, Vol. 32, No. 16, 1995, pp. 2345–2367.

[4]Chattopadhyay, A., and Gu, H., "New Higher-Order Plate Theory in Modeling Delamination Buckling of Composite Laminates,"*AIAA Journal*, Vol. 32, No. 8, 1994, pp. 1709–1716.

[5]Chattopadhyay, A., and Seeley, C. E., "A Higher Order Theory for Modeling Composite Laminates with Induced Strain Actuators," *Composites Part B: Engineering*, Vol. 28B, No. 8, 1997, pp. 243–252.

[6]Mindlin, R. D., "Equations of High Frequency Vibrations of Thermopiezoelectric Crystal Plates," *International Journal of Solids Structure*, Vol. 10, No. 6, 1974, pp. 625–632.

[7]Mukherjee, N., and Sinha, P. K., "A Finite Element Analysis of Thermostructural Behavior of Composite Plates," *Journal of Reinforced Plastics and Composites*, Vol. 12, No. 11, 1993, pp. 1026–1042.

[8]Tauchert, T. R., "Piezothermoelastic Behavior of a Laminated Plate," *Journal of Thermal Stresses*, Vol. 15, No. 1, 1992, pp. 25–37.

[9]Lee, H., and Saravanos, D. A., "Effect of Temperature Induced Material Property Variations on Piezoelectric Composite Plates," *Proceedings of the AIAA/ASME/ASCE/AHS/ASC 37th Structures, Structural Dynamics, and Materials Conference*, AIAA, Reston, VA, 1996, pp. 1781–1788.

[10]Lee, H., and Saravanos, D. A., "Active Compensation of Thermally Induced Bending and Twisting in Piezoceramic Composite Plates," *Proceedings of the AIAA/ASME/ASCE/AHS/ASC 38th Structures, Structural Dynamics, and Materials Conference*, AIAA, Reston, VA, 1997, pp. 120–130.

[11]Chattopadhyay, A., Li, J., and Gu, H., "Coupled Thermopiezoelectric–Mechanical Model for Smart Composite Laminates," *AIAA Journal*, Vol. 37, No. 12, 1999, pp. 1633–1638.

[12]Chattopadhyay, A., Gu, H., and Li, J., "A Coupled Thermo–Piezoelectric–Mechanical Theory for Smart Composites Under Thermal Load," *Proceedings of Ninth International Conference On Adaptive Structures and Technologies*, Boston, 1998, pp. 156–164.

[13]Zhou, X., Chattopadhyay, A., and Gu, H., "Dynamic Response of Smart Composites Using a Coupled Thermopiezoelectric–Mechanical Model," *AIAA Journal*, Vol. 38, No. 10, 2000, pp. 1939–1948.

[14]Zhou, X., and Chattopadhyay, A., "Improved Higher-Order Theory for Laminated Shells Addressing Transverse Stress Continuity," *Proceedings of the AIAA/ASME/ASCE/AHS/ASC 41th Structures, Structural Dynamics, and Materials Conference*, AIAA, Reston, VA, 2001.

[15]Calcote, L. R., *The Analysis of Laminated Composite Structures*, Nostrand Reinhold, New York, 1969.

[16]Zhou, X., Chattopadhyay, A., and Thornburgh, R., "Analysis of Piezoelectric Smart Composites Using a Coupled Piezoelectric–Mechanical Model," *Journal of Intelligent Material Systems and Structures*, Vol. 11, No. 3, 2000, pp. 169–179.

[17]Ray, M. C., Rao, K. M., and Samanta, B., "Exact Solution for Static Analysis of an Intelligent Structure Under Cylindrical Bending," *Computers and Structures*, Vol. 47, No. 6,1993, pp. 1031–1042.

A. M. Baz
Associate Editor